

# Interrelation between $\bar{p}$ -Ca Atom Spectra and Nuclear Density Profiles

Kenta Yoshimura, Shunsuke Yasunaga, and Daisuke Jido  
*Department of Physics, School of Science, Tokyo Institute of Technology, Tokyo 152-8551, Japan*

Junko Yamagata-Sekihara  
*Department of Physics, Kyoto Sangyo University, Kyoto 603-8555, Japan*

Satoru Hirenzaki  
*Department of Physics, Nara Women's University, Nara 630-8506, Japan*  
(Dated: September 4, 2024)

This work studies  $\bar{p}$ -Ca atom spectra in light of the strong shifts and level widths, using the optical model with several types of parametric coefficients. The spectroscopic quantities are obtained as the eigenvalues of the Dirac equation, where the nuclear densities computed via nuclear Density Functional Theory and the effect of the anomalous magnetic moment are incorporated. The results indicate that the isovector term's contribution to the optical potential is crucial for explaining the systematical differences in the strong shifts between  $^{40}\text{Ca}$  and  $^{48}\text{Ca}$ . Furthermore, it is found that both the strong shifts and the level widths exhibit significant dependence on the nuclear density profiles. These findings provide critical insights into the nuclear structures, particularly in the context of Calcium isotopes, by offering a more comprehensive understanding of the underlying nuclear-hadron properties.

## I. INTRODUCTION

Hadronic atoms, which comprise negatively charged mesons or baryons substituting orbiting electrons, represent an intriguing topic within the nuclear-hadron physics, providing deeper insights into the properties of hadrons at finite density [1, 2]. One of the most successful examples is the precise extraction of the in-medium quark condensate from the spectroscopy of deeply bound pionic atoms [3]. Antiprotonic systems are also expected to contain significant features [4–6], such as  $\bar{N}N$  interactions, QED testing and pair-annihilation processes [7–16], where the atomic spectroscopy can offer novel perspectives. Additionally, the rapid advancements in X-ray spectroscopic experiments enable us to deduce not only the intermediate hadron interactions but also nuclear structures [17–28] (and references therein), necessitating more precise investigations from theoretical points of view.

In the contexts of hadronic atoms, one interesting topic is the estimation of the *strong shifts* and *level widths* [29–31], which originate from the strong force and characterize energy level shifts and particle absorptions. These features have been described by the optical model with the aid of the linear density approximation [32–41]. The optical model integrates the strong force by introducing an additional potential  $V_{\text{opt}} = U + iW$ , whose real part leads to the energy shift, while the imaginary part represents the absorption effect. Within the linear density approximation it is assumed that each part of the optical potential depends on a linear combination of neutron and proton densities  $\rho_n$  and  $\rho_p$ , with their coefficients parameterized to match experimental data. Regarding these parameterization, while the relativistic mean-field (RMF) approach [42, 43] has been adopted for investigating deeply bound states [10, 39, 44–48], for level shifts and widths global fittings across wide-range measured atoms have been prevailing [49–52]. For antiprotonic atoms this global fitting protocol with the recent PS209 experiments has been successfully conducted [38–40], concluding that contributions

from neutrons and protons should be symmetric. This indicates that density dependence of the optical potential can be described by solely the isoscalar density  $\rho_0 = \rho_n + \rho_p$ . On the other hand, the experiments have demonstrated significant differences in both shifts and widths among isotope nuclei [53], some of which cannot be explained by the potentials possessing only the isoscalar term, as pointed out in Ref. [23, 54]. This implies that there is a room for including additional contributions to the current optical potential for mentioned isotopes specifically.

The present paper focuses on Calcium isotopes, especially  $^{40}\text{Ca}$  and  $^{48}\text{Ca}$ . Although both are known as double magic nuclei, their properties remain not fully understood. Firstly, whereas in general charge radii swell up as the neutron number increases, the counterparts of these two nuclei are almost identical, exhibiting a “kink” structure in the range of neutron number 40 and 48 [55]. Additionally, there are also discrepancies related to the density distribution, as a recent experimental result has shown that the density profile of  $^{40}\text{Ca}$  is significantly different from any theoretical prediction [56–58]. Investigations of  $\bar{p}$ -atom spectroscopy could provide a novel perspective on this perplexing situation. Our work suggests a theoretical and comprehensive approach to  $\bar{p}$ -atom studies as a tool for the extraction of the nuclear properties. The points which this study focuses on are as follows. In the first place, we examine the role of other terms in the optical potential than the conventional isoscalar term. It is known that there is a systematical difference by a factor of several between the strong shifts of  $^{40}\text{Ca}$  and  $^{48}\text{Ca}$ , although the optical model with the prevailing parameter  $b_0 = (1.5 + 2.5i)$  fm predicts around 3 eV for both of them [54]. This justifies that, at least for Calcium isotopes, the contribution of the isovector  $b_1$  term and/or the p-wave term should be considered in the optical potential. In the second place, more realistic density profiles are adopted in this work. Many of the precedent researches have utilized simple 2-parameter or 3-parameter Fermi (2pF, 3pF) models with phenomenological parameters

such as “skin” or “halo” types [20, 21, 59–63]. This is because, while the proton densities have been precisely obtained through electron scattering experiments [64], it is difficult to get neutron densities directly. For the meanwhile, in the field of nuclear physics, Density Functional Theory (DFT) calculations integrating the Skyrme effective interactions [65, 66] have been successfully developed for the description and prediction of nuclear structures [67]. It is worthwhile investigating how the detailed density profiles impact the spectroscopic observables. In the third place, we consider the effect of the spin-orbit splittings. Within many conventional studies of antiprotonic atoms related to level shifts and widths, calculations have been performed using the Klein-Gordon equation, in which it has been presumed that the spin-orbit splittings are too small to distinguish experimentally. However, due to the large anomalous magnetic moment of antiprotons, a planned high-resolution X-ray spectroscopic experiment with a state-of-the-art quantum sensor [68] could separate the split energy levels. A proper quantum mechanical treatment of spin 1/2 fermions is the Dirac equation, whereby the spin-orbit interaction is inherently taken into account.

In this context, we develop a calculation framework based on the Dirac equation, integrating the optical model and the effect of the anomalous magnetic moment. In the calculations, we assume the spherical symmetry taking into account the sphericity of both  $^{40}\text{Ca}$  and  $^{48}\text{Ca}$ , leading to lower computational cost. For the density profiles, we calculate densities using not only the simple 3pF model, but also the DFT models with several parameter sets. The coefficients for the optical potential have been prepared referring to some of the precedent researches, where they have dealt with the global fitting in alignment with the experimental data [1, 38]. Because the lowest state dominantly observed in X-ray spectroscopy is the  $(n, l) = (5, 4)$  state for Ca isotopes [54], in this paper we focus on the properties of  $n = 5$  and  $n = 6$  orbits. By comparing the results with various density profiles and optical potential models, we investigate how nuclear structures and potential shapes influence spectroscopic quantities such as strong shifts and level widths.

The arrangement of this article is as follows. Section II explains the formalism and methodologies used in this work. Section III presents and discusses the calculation results. Section IV summarizes the work and provides the future prospects.

## II. FORMALISM

This section formulates the equation of motion (EoM) for the  $\bar{p}$ -Ca atomic systems. The EoM is expressed as Dirac equation, incorporating both the electromagnetic potential and the optical potential representing the effect of the strong interaction. For the optical potential, it is necessary to assume the shape of the potentials with its parametric coefficients and nuclear properties. In this work we consider three models referring to the precedent research. While physical quantities regarding the nuclear structures are adopted from the experimental data, the density profiles are given by the 3pF model and nuclear DFT. In our calculations the EoM is written down

into the matrix representation in the coordinate space, and the energy eigenvalues are obtained by diagonalization methods.

### A. Dirac equation

When the scalar potential  $S(\mathbf{r})$  and 0-th component of the vector potential  $V_0(\mathbf{r})$  are present, the Dirac Equation for 4-spinor  $\psi(\mathbf{r})$  at a fixed energy  $E$  is written as

$$\left( -i\boldsymbol{\alpha} \cdot \nabla + \beta(m + S) + V_0 - \frac{i\kappa}{2m} \frac{dV_0}{dr} \boldsymbol{\gamma} \cdot \hat{\mathbf{r}} \right) \psi = E\psi, \quad (1)$$

where the Pauli term with the anomalous magnetic moment  $\kappa = 1.79284734$  is taken into account [69]. In the standard representation of the Dirac matrices, we have

$$\begin{aligned} \boldsymbol{\alpha} &= \begin{pmatrix} 0 & \boldsymbol{\sigma} \\ \boldsymbol{\sigma} & 0 \end{pmatrix}, \\ \beta &= \begin{pmatrix} 1 & 0 \\ 0 & -1 \end{pmatrix}, \\ \boldsymbol{\gamma} &= \begin{pmatrix} 0 & \boldsymbol{\sigma} \\ -\boldsymbol{\sigma} & 0 \end{pmatrix}. \end{aligned} \quad (2)$$

When both of the potential  $S$  and  $V_0$  are spherically symmetric, the wave function  $\psi$  can be labeled by total angular momentum  $j$ , orbital angular momentum  $l$  and azimuthal angular momentum  $m$ . Here, from the composition of orbital angular momentum and spin-1/2,  $l$  takes the value of either  $j + 1/2$  or  $j - 1/2$  for given  $j$ . Thus, we use the shorthand notation  $(\pm)$  for the case  $l = j \pm 1/2$ , respectively. The wave function  $\psi$  can be separated into radial and spherical variables as follows:

$$\psi_{jm}^{(\pm)}(\mathbf{r}) = \begin{pmatrix} i \frac{G_j^{(\pm)}(r)}{r} \mathcal{Y}_{jm}^{(\pm)}(\theta, \phi) \\ \frac{F_j^{(\pm)}(r)}{r} (\boldsymbol{\sigma} \cdot \hat{\mathbf{r}}) \mathcal{Y}_{jm}^{(\pm)}(\theta, \phi) \end{pmatrix}, \quad (3)$$

where  $\mathcal{Y}_{jm}^{(\pm)}$  is the spinor spherical harmonics defined as

$$\mathcal{Y}_{jm}^{(\pm)} = \begin{pmatrix} \langle (\pm), m - \frac{1}{2}, \frac{1}{2}, +\frac{1}{2} | j, m \rangle Y_{(\pm), m - \frac{1}{2}} \\ \langle (\pm), m + \frac{1}{2}, \frac{1}{2}, -\frac{1}{2} | j, m \rangle Y_{(\pm), m + \frac{1}{2}} \end{pmatrix}. \quad (4)$$

Under this variable separation, the EoM for the radial directions can be written as

$$\begin{aligned} (E - m - S(r) - V_0(r))G_j^{(\pm)}(r) \\ = -\frac{dF_j^{(\pm)}(r)}{dr} \pm \left( j + \frac{1}{2} \right) \frac{F_j^{(\pm)}(r)}{r} - \frac{\kappa}{2m} \frac{dV_0}{dr} \frac{F_j^{(\pm)}(r)}{r}, \\ (E + m + S(r) - V_0(r))F_j^{(\pm)}(r) \\ = \frac{dG_j^{(\pm)}(r)}{dr} \pm \left( j + \frac{1}{2} \right) \frac{G_j^{(\pm)}(r)}{r} - \frac{\kappa}{2m} \frac{dV_0}{dr} \frac{G_j^{(\pm)}(r)}{r}. \end{aligned} \quad (5)$$

Given the two-body systems with masses  $m_A$  and  $m_B$ , and the interactions exclusively depending on the relative distance between them, the EoM can be divided into the center of the

mass part and the relative coordinate part. For the latter part, the form of the EoM is the same with the original Dirac equation (5), except that the mass term is replaced by the *reduced mass*, written as

$$\mu = \frac{m_A m_B}{m_A + m_B}. \quad (6)$$

In the following formulations, we implicitly assume that the spherical symmetry holds in interested systems, and the coordinate  $r$  always stands for the relative distance between the center of mass of two particles, namely the Ca nuclei and antiprotons.

### B. Coulomb Potential

In the  $\bar{p}$ -Ca atomic systems, the 0-th component of the vector potential  $V_0$  contains the electromagnetic potential  $-eA_0$  in the Coulomb gauge:

$$-eA_0(r) = -\alpha \int d^3\mathbf{r}' \frac{\rho_p(r')}{|\mathbf{r} - \mathbf{r}'|}, \quad (7)$$

where  $\alpha = e^2/4\pi\epsilon_0 = 1/137.036$  is the fine structure constant and  $\rho_p$  is the proton density which is given later. With the integral for elevation and azimuth angle components performed, it turns into

$$-eA_0(r) = -\frac{2\pi\alpha}{r} \int_0^\infty dr' r' \rho_p(r') (r + r' - |r - r'|). \quad (8)$$

In our framework, we consider the effect of the vacuum polarization up to the first-leading  $Z\alpha^2$  order. Let us write this contribution as  $V_{VP}$  given by

$$V_{VP}(r) = -\frac{2}{3} \frac{\alpha^2}{m_e r} \int_0^\infty dr' r' \rho_p(r') [f(|r - r'|) - f(r + r')], \quad (9)$$

with

$$f(r) = \int_1^\infty dt e^{-2m_e r t} \left( \frac{1}{t^3} + \frac{1}{2t^5} \right) \sqrt{t^2 - 1}, \quad (10)$$

which corresponds to  $K_0(x)$  in Ref. [70] and where  $m_e$  is the electron mass. Finally the vector potential can be written as

$$V_0(r) = -eA_0(r) + V_{VP}(r). \quad (11)$$

Although, in Ref. [71], it has been pointed out that the higher order of the vacuum polarization may change the binding energies by several percent, in the present paper this effect is neglected. This is because we calculate the energy shifts by the strong interaction which are given by the difference between the binding energies with and without the optical potential and thus this difference should not be affected largely by the detail shapes of Coulomb potential. This is also the case for the level widths because they solely depend on the imaginary part of the optical potential.

### C. Optical Potential

In our framework, the optical potential is contained in the scalar potential  $S(r)$ . As explained previously, within the framework of the linear density approximation, the optical potential can be represented as a linear combination of the nuclear (neutron and proton) densities  $\rho_n(r)$  and  $\rho_p(r)$ :

$$S(r) = [B_n \rho_n(r) + B_p \rho_p(r)] + \nabla [C_n \rho_n(r) + C_p \rho_p(r)] \cdot \nabla. \quad (12)$$

A generic form of the optical potential has the following form:

$$S(r) = -\frac{4\pi}{2\mu} \left( 1 + \frac{\mu}{M_N} \right) [b_0 \rho_0(r) + b_1 \rho_1(r)] + \frac{4\pi}{2\mu} \left( 1 + \frac{\mu}{M_N} \right)^{-1} \nabla [c_0 \rho_0(r) + c_1 \rho_1(r)] \cdot \nabla, \quad (13)$$

with the isoscalar  $\rho_0$  and isovector density  $\rho_1$  written as

$$\rho_0(r) = \rho_n(r) + \rho_p(r), \quad (14)$$

$$\rho_1(r) = \rho_n(r) - \rho_p(r), \quad (15)$$

and the averaged nucleon mass  $M_N = 938.918$  MeV. The terms in the first and second braces represent the s-wave and p-wave components of the relative partial wave, respectively, whose detailed derivation is explained in Ref. [32, 33]. The coefficients  $b_0, b_1, c_0, c_1$  should originally be connected to the scattering lengths and volumes of  $\bar{N}N$  scatterings by means of the  $t\rho$  approximation, and can be calculated for example by Paris potential [36, 41, 72–74]. However, it is known that potentials derived from these theories do not accurately reproduce experimental results for  $\bar{p}$  atoms, therefore it is common practice to treat these coefficients as free parameters which should be fitted to match the experimental data. Many parameters have been advocated, and in the modern context, global fittings have referred to the latest PS209 experiments [39, 53], reaching a consensus that neither the isovector part nor p-wave component contribute significantly. In this paper, however, we employ the optical potentials with these expelled components, and also consider the point-coupling interactions between the antiprotons and nucleus for simplicity, which is contrary to the convention [35, 40] This is because in this work we are not interested in a quantitatively precise prediction of the  $\bar{p}$ -Ca spectroscopy, but in the systematical relationships between the optical models and the physical quantities. In this sense this treatment of optical potentials should be justified, and for this purpose we employ characteristic a few parameter sets, which are exhibited in Table. I. All parameter sets have the same value for the  $b_0$  term, which is adopted from Ref. [1]. The difference is whether the isovector or p-wave term is included or not, and their values are also referring to Ref. [1, 38]. They should enable us to extract the role of each term integrated in the optical potential.

### D. Nuclear Properties

To perform the calculations and extract the quantitative observables from the above formalism, we need the information

TABLE I. The optical potential parameter sets used in this work.

	$b_0(\text{fm})$	$b_1(\text{fm})$	$c_0(\text{fm}^3)$
Type I	$2.5 + 3.4i$	-	-
Type II	$2.5 + 3.4i$	$-14.0 + 5.0i$	-
Type III	$2.5 + 3.4i$	-	$-4.0 - 2.5i$

TABLE II. Parameters for the 3pF model in  $^{40}\text{Ca}$  and  $^{48}\text{Ca}$ , with simplified neutron skin thickness. From left to right, the mass of nuclei  $M_{\text{Ca}}$ , the proton mean radius  $R_p$ , diffuseness  $a$ ,  $w$ , and the neutron mean radius  $R_n$  are exhibited.

	$M_{\text{Ca}}(\text{MeV})$	$R_p(\text{fm})$	$a(\text{fm})$	$w$	$R_n(\text{fm})$
$^{40}\text{Ca}$ 3pF	37214.698	3.766	0.586	-0.161	3.766
$^{48}\text{Ca}$ 3pF-2.0	44657.272	3.7369	0.5245	-0.03	3.9369
3pF-2.5					3.9869
3pF-3.0					4.0369

on the nuclear properties. Among them, the masses of nuclei  $M$  and each nucleus  $M_{\text{Ca}}$  are experimentally evaluated and available in Ref. [75]. On the other hand, there are several different models for nuclear densities, especially neutron densities. Conventionally used has been the 3pF model where the density is simply represented by

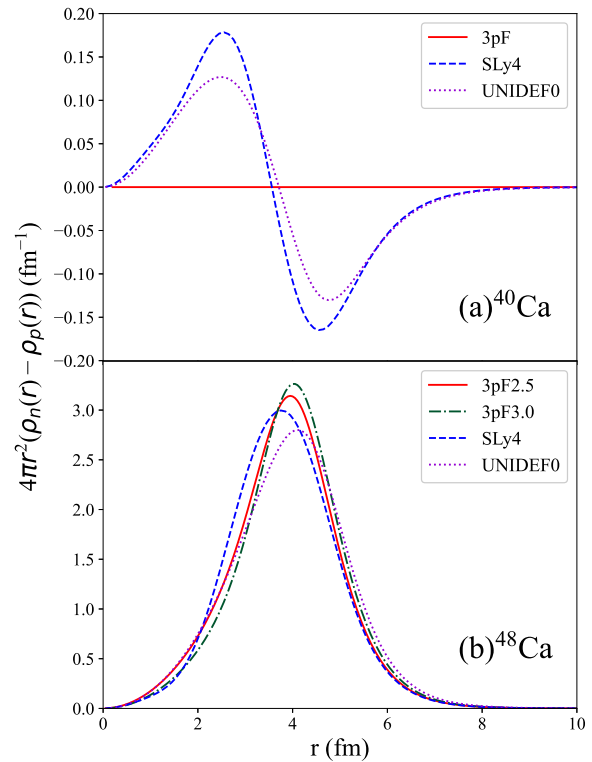
$$\rho_q(r) = \left(1 + w \frac{r^2}{R_q^2}\right) \frac{\rho_c}{1 + \exp((r - R_q)/a)}, \quad (16)$$

with particle species  $q = n, p$  and parameters  $w$ ,  $R_q$  and  $a$ . The parameter  $R_q$  stands for the nuclear radius and should be evaluated for neutrons and protons, respectively, while  $\rho_c$  is the normalization factor which should be determined consistently with the total particle numbers through

$$\int 4\pi r^2 \rho_q(r) dr = N_q. \quad (17)$$

TABLE III. A comparison table of proton and neutron mean radii for both  $^{40}\text{Ca}$  and  $^{48}\text{Ca}$ , with densities calculated by the 3pF model with empirical parameters, or by the DFT model with several profiles. All the quantities are in a unit of fm.

	$^{40}\text{Ca}$			$^{48}\text{Ca}$		
	$r_n$	$r_p$	$\Delta r_{np}$	$r_n$	$r_p$	$\Delta r_{np}$
3pF-2.0	3.482	3.482	0.00	3.600	3.469	0.130
3pF-2.5	3.482	3.482	0.00	3.633	3.469	0.163
3pF-3.0	3.482	3.482	0.00	3.665	3.469	0.196
SLy4	3.373	3.421	-0.047	3.607	3.454	0.153
SLy5	3.369	3.417	-0.048	3.612	3.452	0.160
SkM*	3.378	3.437	-0.049	3.602	3.447	0.155
SAMi	3.344	3.391	-0.047	3.615	3.440	0.174
SGII	3.349	3.399	-0.050	3.583	3.436	0.147
UNEDF0	3.384	3.426	-0.042	3.647	3.438	0.209
UNEDF1	3.363	3.399	-0.036	3.620	3.436	0.184
UNEDF2	3.352	3.389	-0.036	3.598	3.431	0.167
HFB9	3.377	3.424	-0.047	3.607	3.450	0.157

FIG. 1. The isovector density  $\rho_1$  as a function of the radial coordinate, with respect to several density profiles. In the upper panel, distribution of  $^{40}\text{Ca}$  is exhibited, and the lower shows that of  $^{48}\text{Ca}$ .

Whereas the proton radius  $R_p$  is well known thanks to electron scattering experiments, there is a little information on neutron radius  $R_n$ , which necessitates to assume the phenomenological function form. For  $^{40}\text{Ca}$ , a symmetric nucleus, we can assume that the neutron and proton densities are identical as a good approximation. However, for neutron-rich  $^{48}\text{Ca}$ , such an assumption may not be considered realistic, due to the existence of the neutron “skin” at the nuclear surface. Regarding the neutron skin thickness, there is still a room for discussion, so that in this work, we prepare three models for  $R_n$ , which we call 3pF-2.0, 3pF-2.5, 3pF-3.0, respectively. In Table II, the parameters for  $^{40}\text{Ca}$  and  $^{48}\text{Ca}$  are exhibited. The masses of nuclei are adopted from [75], and the others except the neutron radii  $R_n$  are referring to [64]. As explained above, for  $^{40}\text{Ca}$  we set the neutron radius as  $R_n = R_p$ , and for 3pF-X.X of  $^{48}\text{Ca}$ , we set  $10(R_n - R_p) = \text{X.X}$ .

In addition to the 3pF model, we employ more realistic density distributions obtained through the nuclear DFT calculations [66]. Within the DFT framework, the ground state is calculated according to the variational principle of the energy density functionals (EDFs), with several parameter sets. There exist a lot of parameter sets in accordance with their dedicated experimental database, and we adopt several representative parameter sets of the Skyrme-type EDF [66]; SLy4 [76], SLy5 [76], SkM\* [77], SAMi [78], SGII [79], UNEDF0 [80], UNEDF1 [81], UNEDF2 [82], HFB9 [83]. With these parameters, we perform the Hartree-Fock-Bogoliubov calculation with assuming the spherical symmetry [84]. We use the

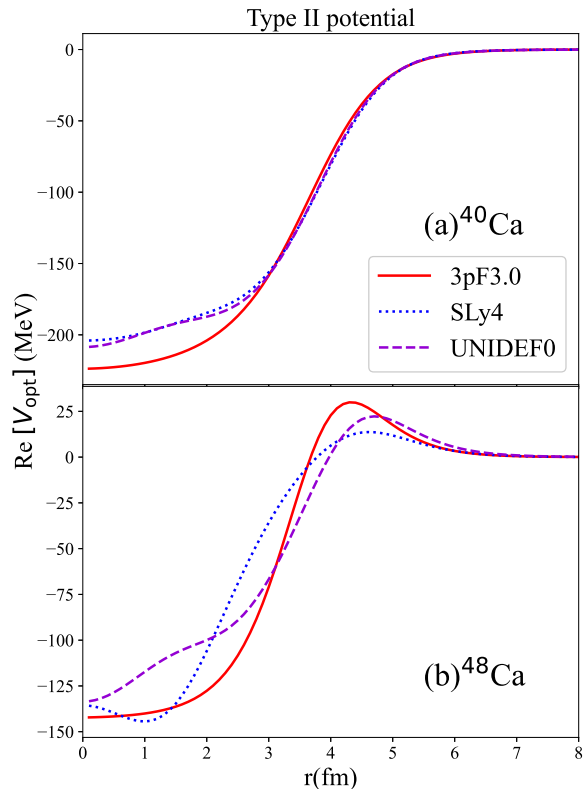


FIG. 2. The real part of the optical potential with Type II parameters as a function of the radial coordinate, for several representative of the nuclear profiles. In the upper panel, distribution of  $^{40}\text{Ca}$  is exhibited, and the lower shows the counterpart of  $^{48}\text{Ca}$ .

volume-type pairing interaction, whose strengths are given in Ref. [55]. They give different proton and neutron root-mean-square (RMS) radii as well as density profiles, which are summarized in Table III.

Figure 1 shows the isovector densities  $\rho_1 = \rho_n - \rho_p$  for  $^{40}\text{Ca}$  and  $^{48}\text{Ca}$  in the upper and lower panels, respectively. For  $^{40}\text{Ca}$ , the density of the 3pF model is always zero, which is natural because all the parameters are same, while the counterparts of the Skyrme model go to negative at the surface. For  $^{48}\text{Ca}$ , although isovector densities are always positive for all density profiles, the position and height of peaks differ, which should lead to the significant variety of the Type II optical potential. Figure 2 demonstrates the shape of the real part of the optical potential with the Type II potential, for several representative density profiles. From this figure, one can find two characteristic behaviours. In the first place, for  $^{40}\text{Ca}$ , density profiles in case of DFT make the potential shallower in the center region. This point itself seems to affect nor the strong shifts neither level widths, because the  $\bar{p}$ -atom spectra are considered to depend on only the nuclear periphery structures. However, the depth of the potential may alter the level structures of deeply bound states, which could lead to the shift of the atomic states through the level repulsion. In the second place, for  $^{48}\text{Ca}$ , their density distributions are totally different. In the periphery region, it is found that the potentials change to repulsive, due to the negative value of  $\text{Re}\{b_1\}$ . The

magnitude of these repulsive regions is significantly different among the density profiles, which should impact the spectroscopic observables quantitatively.

### E. Computation Method

In the present work, the energy eigenvalues  $E$ , generally complex numbers, of the Dirac equation (5) are calculated via matrix diagonalizations of the Hamiltonian matrix for the radial wave functions  $F(r)$  and  $G(r)$ . For the bound states, the obtained eigenenergies can be connected to the binding energy  $B$  and the absorption width  $\Gamma$ , by using the following relation:

$$E = \mu - B - i\frac{\Gamma}{2}. \quad (18)$$

Because both the reduced mass  $\mu$  and binding energy  $B$  are always real, the absorption width can be easily obtained from the imaginary part of the energy eigenvalues. On the other hand, the strong shifts cannot be obtained directly, as they represent the difference in binding energies calculated with and without the optical potential. Let us define the binding energy with the optical potential as  $B_{w/o,opt}$  and without the optical potential  $B_{w/o}$ . The strong shift  $\varepsilon$  is calculated by

$$\varepsilon = B_{w/o} - B_{w/o,opt}. \quad (19)$$

For constructing the Hamiltonian matrix, we employ the finite difference method (FDM), in which the radial coordinate space is discretized into  $N_r$  grid points with spacing  $\Delta r$ . The size of the cell  $R_{\text{max}}$  is determined by  $R_{\text{max}} = N_r \Delta r$ . Because atomic orbits extend far outside nuclei, a small cell size may conflict with the boundary condition  $F(r)|_{r=\infty} = G(r)|_{r=\infty} = 0$ , leading to fluctuations in both the wave functions and energy eigenvalues. We verify that the setting  $N_r = 1200$  and  $\Delta r = 0.2$  fm provides good convergence for any bound state examined.

## III. RESULTS AND DISCUSSION

In this section, we show the calculation results. Our discussing issues are mainly three-folds; 1. What optical model can reproduce the systematical differences of strong shifts and level widths between  $^{40}\text{Ca}$  and  $^{48}\text{Ca}$ , 2. how the density profiles impact the  $\bar{p}$ -Ca atom spectroscopy, 3. whether the spin-orbit splitting can be distinguished experimentally, under the effect of the anomalous magnetic moment. All these issues will be thoroughly reviewed separately in this section. While the tables of the calculation results are arranged in align with each dedicated subsection, the full set of results can be seen in Appendix A.

### A. Pure Electromagnetic States

First of all, we show the calculation results of the binding energies in Table IV without the optical potential imple-

mented. For comparison, we juxtapose the calculated binding energies by means of the exact solution from the point Coulomb potential, which is represented by

$$E_{nj}^{\text{PC}} = \mu \left[ 1 + \frac{Z^2 \alpha^2}{\left\{ n - j - \frac{1}{2} + \sqrt{\left( j + \frac{1}{2} \right)^2 - Z^2 \alpha^2} \right\}^2} \right]^{-1/2} \quad (20)$$

with the principle quantum number  $n$  and total angular momentum  $j$ . From Tab. IV, it is found that the calculated binding energies are sufficiently consistent with the analytical solution, which ensures the validity of our calculation framework. The difference from the point-Coulomb results is generally around zero point several percent, which can be attributed to the effect of the anomalous moment. This is because the calculated energies of both spin states are shifting in a direction that enhances the magnitude of the spin-orbit splitting. This point will be discussed to be detailed in the later section.

TABLE IV. The calculated binding energies of  $(n, l) = (5, 4)$  and  $(6, 5)$  states for  $^{40}\text{Ca}$  and  $^{48}\text{Ca}$ , by means of our suggesting framework, as well as the point-Coulomb potential. The optical potential is not included, and all energies are in a unit of keV.

	$^{40}\text{Ca}$		$^{48}\text{Ca}$	
	calc.	PC	calc.	PC
$5g_{9/2}$	389.852	389.967	391.431	391.572
$5g_{7/2}$	390.233	390.050	391.814	391.656
$6h_{11/2}$	270.759	270.793	271.856	271.907
$6h_{9/2}$	270.906	270.825	272.004	271.940

## B. Optical Model Comparison

Table V shows the strong shift for  $n = 5$  and the level width for  $n = 6$  for each optical model. Here we note that the case where the strong shift  $\epsilon > 0$  indicates the repulsive shift, and the negative  $\epsilon$  means the attractive shift. The results for  $^{40}\text{Ca}$  are shown in the second and third columns, and the counterparts for  $^{48}\text{Ca}$  are exhibited in the fourth and fifth columns. The models of the density profiles are 3pF and 3pF-3.0 for  $^{40}\text{Ca}$  and  $^{48}\text{Ca}$ , respectively. Additionally, the experimental results provided in [54] are listed in the bottom row. Even though the measurement errors are somewhat large, characteristic is the systematical difference between  $^{40}\text{Ca}$  and  $^{48}\text{Ca}$  in both the strong shifts and level widths. As is explained in introduction, it has been pointed out that the currently prevailing model with only the isoscalar term  $b_0 = (1.5 + 2.5i)$  fm does not reproduce this experimental results, yielding around 3 eV and similar in any calculation setting [54]. The present work's results demonstrate that the Type I potential also results in around 3-4 eV strong shifts, which is consistent with the mentioned paper [54]. Additionally, the Type III model also fails to reproduce both the shift and width difference, with overestimating the shift of  $^{40}\text{Ca}$ . From this result it is proposed

TABLE V. The strong shift for  $n = 5$  and level width for  $n = 6$  in a unit of eV, with respect to optical parameter sets. The second to the third column, the result of  $^{40}\text{Ca}$  is provided, for the 3pF density. The fourth to fifth column exhibit the counterpart of  $^{48}\text{Ca}$  with the 3pF-3.0 density. At the bottom line the experimental result[54] is shown.

	$^{40}\text{Ca}$		$^{48}\text{Ca}$	
	$\epsilon_{n=5}$	$\Gamma_{n=6}$	$\epsilon_{n=5}$	$\Gamma_{n=6}$
Type I	2.85	0.121	3.56	0.170
Type II	2.85	0.121	22.5	0.165
Type III	25.9	0.058	31.1	0.063
Exp.	5(12)	0.059(18)	33(12)	0.116(17)

that the p-wave component of the optical potential be not significantly large for Calcium isotopes. The Type II potential, even though it does not explain the Ca experimental results quantitatively, the systematical differences between two nuclei are most accurately replicated. Consequently it is inferred that, contrary to the present consensus in the global fitting, the isovector term needs to exist with a sufficiently large value for well describing the experimental data, at least regarding Calcium isotopes. Although there is still a quantitative deviation, it could be improved by elaborate fitting processes, and additionally, as will be shown in the following sections, the adopted density profiles may alter both the shifts and widths significantly.

## C. Density Profile Comparison

In Table VI, we show the comparative results of the level shifts of  $n = 5$  and widths of  $n = 6$ , with respect to each density profile, and with the Type II optical potential. The second to fifth columns indicate the values for  $^{40}\text{Ca}$ , and right three ones are dedicated to  $^{48}\text{Ca}$ . The neutron skin thickness  $\Delta r_{np}$  is also presented next to the calculation results. From this table one finds that, even if the magnitude of  $\Delta r_{np}$  is comparable, both the strong shifts and widths can be significantly different, and particularly for  $^{48}\text{Ca}$ , the difference reaches a few tens percent among the different density profiles. For visibility, in Fig. 3, calculated values are plotted as a function of neutron skin thickness, for  $^{48}\text{Ca}$  and with the type II potential. Each point is labeled by the name of its density profile. From this figure it is found that the results of the 3pF calculations for both strong shift and level width gain almost linearly as neutron skin thickness swells up. On the other hand, no such simple trend can be read from the calculation results with DFT-based density profiles. Furthermore, from this figure, it is found that the 3pF results underline in the strong shifts, while overline in the widths. This implies the necessity to take into account the realistic density profiles beyond the 2pF or 3pF models, for the quantitatively precise prediction of the  $\bar{p}$ -Ca spectroscopy.

TABLE VI. A comparative result of the neutron skin thickness, strong shifts, and level widths, with respect to density profiles. For all the results Type II parameter is incorporated. The second to fourth, and fifth to seventh columns show the result of  $^{40}\text{Ca}$  and  $^{48}\text{Ca}$ , respectively. The neutron skin thickness is in a unit of fm, while the others are in eV.

	$^{40}\text{Ca}$			$^{48}\text{Ca}$		
	$\Delta r_{np}$	$\varepsilon_{9/2}$	$\Gamma_{11/2}$	$\Delta r_{np}$	$\varepsilon_{9/2}$	$\Gamma_{11/2}$
3pF-2.0	0.0	2.85	0.121	0.130	18.5	0.155
3pF-2.5	-	-	-	0.163	20.5	0.160
3pF-3.0	-	-	-	0.196	22.5	0.165
SLy4	-0.047	-1.52	0.077	0.153	22.1	0.119
SLy5	-0.048	-1.58	0.077	0.160	22.9	0.124
SkM*	-0.049	-2.06	0.080	0.155	21.2	0.115
SAMi	-0.047	-1.42	0.070	0.174	24.1	0.126
SGII	-0.050	-2.21	0.074	0.147	20.3	0.112
UNEDF0	-0.042	-2.31	0.080	0.209	28.6	0.144
UNEDF1	-0.036	-2.17	0.075	0.184	28.3	0.143
UNEDF2	-0.036	-1.93	0.071	0.167	25.0	0.125
HFB9	-0.047	-2.27	0.079	0.157	22.9	0.121

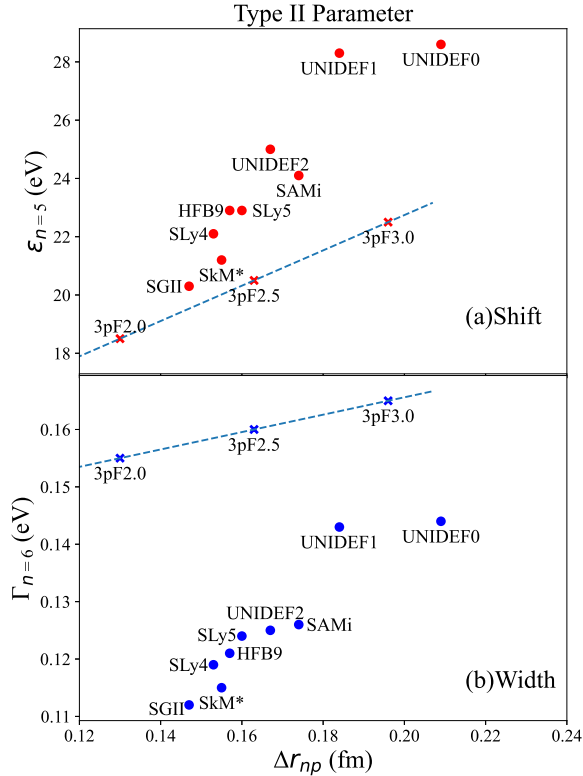


FIG. 3. Scatter plots of the calculated values for  $^{48}\text{Ca}$ , with Type II parameter, as functions of the neutron skin thickness. Each point is labeled by used density profiles. The upper and lower panel demonstrates the result of shifts and widths, respectively.

## D. Nuclear State Effect

Another interesting feature can be revealed from the Table VI. From strong shifts of  $^{40}\text{Ca}$  with the type II parameter, it is found that their signs are reversed from the 3pF model to other density distributions. It seems a little bit weird, because the optical potential of  $^{40}\text{Ca}$  is, as is shown in Fig. 2, always attractive, which apparently does not contribute to repulsive shifts. This feature can be explained by examining the ‘‘Nuclear’’ states, namely the deeply bound states in the nuclear potential. The effect of nuclear states on the atomic spectra has been already discussed in Ref. [85], where it has been pointed out that the existence of nuclear states brings about the dispersion behaviour in the strong shifts and widths. Table VII lists the binding energies for several density distributions in  $^{40}\text{Ca}$  with Type II parameters. As can be seen, the 3pF model has a shallow bound orbital with several MeV that does not appear in other density distributions. This can be attributed to the lift down of the optical potential in the center region, which can be seen in Fig 2. This shallow bound states are inferred to contribute to level repulsion with the next higher atomic bound orbital, resulting in a slight shift of the binding energies. The diagonalization method, provides all possible states without any prior bias, which enables us to discuss the energy level structures from multi-dimensional perspectives. Additionally, this feature suggests that the shape of the optical potential can alter the value of the strong shift, due not only to its periphery structure but also to the behaviour in its center region. This point should throw a stark light on the current framework of the  $\bar{p}$ -atom spectroscopy.

TABLE VII. The binding energies for  $j = 9/2$  states of  $^{40}\text{Ca}$ , with Type II optical potential and several representative density profiles. All the energies are indicated in a unit of keV. ‘‘Nucl’’ means that the corresponding orbits are bound inside the nuclear potential, and ‘‘Atom’’ is outside.

	3pF	SLy4	SAMi	UNEDF0
Nucl 1	78705	69556	73338	72910
Nucl 2	3871.0	-	-	-
Atom 1	389.86	389.83	389.83	389.83

## E. Spin-orbit Splitting

Figure 4 shows the level transition scheme for  $\bar{p}$ - $^{40}\text{Ca}$  and  $\bar{p}$ - $^{48}\text{Ca}$ , while the values of the transition energies from the yrast  $n = 6$  to  $n = 5$  states are demonstrated in Tab. VIII. Without considering the spin-flip transitions, the spin-orbit splittings should be observed as distinguished peaks with different spins. These figure and table reveal that the magnitude of the spin-orbit splittings are around 235 eV for both nuclei, which could be separated with the state-of-the-art high-resolution X-ray spectroscopy. Furthermore, it is found that the transition energies are almost unchanged by choice of density profiles or optical potentials, which indicates that the scale of spin-orbit splittings is not affected by detail of the potential shapes.

Additionally, we note that they could not be observed experimentally until the effect of the anomalous magnetic moment is considered. This is because with the Pauli approximation the transition energies can be written as

$$\Delta E_{nj} \approx (1 + 2\kappa) \frac{\mu c^2}{2} \frac{(Z\alpha)^4}{n^3 l(l+1)}, \quad (21)$$

which is explicitly proportional to  $(1 + 2\kappa)$ . The anomalous moment of antiproton is approximately  $\kappa \sim 1.8$ , which leads to the gain of the spin-orbit splittings by a factor of 4.6. Without this effect the value of the splittings is around 50 eV, which should be obscured in the level widths of  $n = 5$  states.

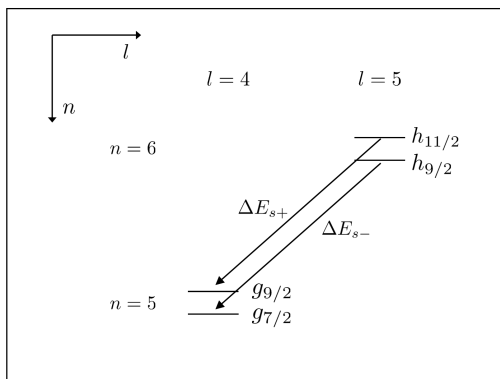


FIG. 4. Level transition scheme in  $\bar{p}^{40}\text{Ca}$  and  $\bar{p}^{48}\text{Ca}$ .

#### IV. SUMMARY

In this work, a comprehensive study in the  $\bar{p}$ -Ca atom spectroscopy has been conducted based on the Dirac equation with optical potentials which include the isovector or p-wave components as well as with realistic density profiles via the nuclear DFT calculations incorporated. By comparing the strong shifts and level widths associated with these optical potentials, our analysis suggests that elucidating their systematic differences between  $^{40}\text{Ca}$  and  $^{48}\text{Ca}$  necessitates the inclusion of the isovector  $b_1$  terms with sufficiently large values. Furthermore, systematic calculations across a variety of density profiles have demonstrated that, despite using identical optical models, both shifts and widths exhibit a significant difference, sometimes by a few tens of percent. This difference can be attributed not merely to quantitative alterations in nuclear structures but also to the specific level structures of deeply bound

states, as pointed out in Ref. [85]. These findings suggest that the density profiles play a critical role in the antiprotonic atom spectra. Moreover, differences in binding energies obtained through the diagonalization of the Hamiltonian matrix, reveal that the spin-orbit splitting possesses a substantial magnitude of several hundred eV, which can be resolved by contemporary high-precision X-ray spectroscopy experiments.

These results serve as a strong tool for accurately investigating the nuclear structure of Ca isotopes from the perspective of the antiprotonic atoms. The state-of-the-art X-ray experiments undoubtedly provide much more accurate information about the  $\bar{p}$ -Ca spectroscopy, which leads to the understandings of the optical potential type as well as the nuclear structure. Moreover, given that the isovector term is revealed to play an important role as indicated in this study, this should also pave a way for the precise determination of the neutron skin thickness. As a future prospect, we can extend the developed framework to other Calcium isotopes such as  $^{42,44,46}\text{Ca}$ . Given that the validity of such studies is revealed, we can apply this framework to other atomic nuclei for the investigation of their nuclear structures, which comprehensively facilitates the liaison between the hadron physics and nuclear physics.

#### ACKNOWLEDGEMENT

We would extend gratitude to Hiroyuki Fujioka for valuable discussions and providing knowledge from the experimental field. We would also thank Tomoya Naito for offering calculation data of density distributions. This work partly made use of computational resources of the Yukawa-21 supercomputer at Yukawa Institute for Theoretical Physics (YITP), Kyoto University. One of the authors (K.Y.) would like to acknowledge the financial support from the JSPS Research Fellow, Grant No. 24KJ1110. The work of D.J. was partly supported by Grants-in-Aid for Scientific Research from JSPS (21K03530, 22H04917, 23K03427).

#### Appendix A: Full Set of Calculation Results

Table IX to XII show the full set of calculation results for strong shifts  $\varepsilon$  and level widths  $\Gamma$  of  $5g_{9/2}$ ,  $5g_{7/2}$ ,  $6h_{11/2}$  and  $6h_{9/2}$  states. From these tables, it is clear that both the strong shifts and level widths do not change between the different spin states, which is why in the body the spin dependence of the spectroscopy has not been particularly discussed. In addition, the level widths for  $n = 5$  states are around 30-40 eV, which is more or less consistent with a weighted average of 35(6) eV for  $^{40,42,43,44,48}\text{Ca}$  [54].

- [1] C. J. Batty, E. Friedman, and A. Gal, *Physics Reports* **287**, 385 (1997).
- [2] E. Friedman and A. Gal, *Physics Reports* **452**, 89 (2007).
- [3] T. Nishi *et al.* (piAF Collaboration), *Nat. Phys.* **19**, 788 (2023).
- [4] C. J. Batty, *Rep. Prog. Phys.* **52**, 1165 (1989).

- [5] E. Klempt, C. Batty, and J.-M. Richard, *Physics Reports* **413**, 197 (2005).
- [6] M. Doser, *Progress in Particle and Nuclear Physics* **125**, 103964 (2022).
- [7] S. Wycech, *Nuclear Physics A* **692**, 29 (2001).

TABLE VIII. The energy differences of the  $\bar{p}6 \rightarrow 5$  transitions.  $\Delta E_{s+}$  denotes the transition from  $6h_{11/2}$  to  $5g_{9/2}$ , while  $\Delta E_{s-}$  is for  $6h_{9/2}$  to  $5g_{7/2}$  transition. The difference between  $\Delta E_{s+}$  and  $\Delta E_{s-}$  is also demonstrated as  $\Delta E_{\pm}$ . All the energies are exhibited in unit of keV. In the ‘‘3pF’’ column, for the density profile of  $^{48}\text{Ca}$  the 3pF-3.0 is adopted.

	$^{40}\text{Ca}$			$^{48}\text{Ca}$		
	$\Delta E_{s+}$	$\Delta E_{s-}$	$\Delta E_{\pm}$	$\Delta E_{s+}$	$\Delta E_{s-}$	$\Delta E_{\pm}$
pure e.m.						
3pF	119.093	119.327	0.234	119.575	119.810	0.235
SLy4	119.094	119.328	0.234	119.584	119.819	0.235
UNEDF0	119.094	119.328	0.234	119.584	119.819	0.235
w/ Type II opt.						
3pF	119.102	119.336	0.234	119.562	119.797	0.235
SLy4	119.096	119.330	0.234	119.562	119.797	0.235
UNEDF0	119.096	119.331	0.235	119.556	119.791	0.235

TABLE IX. The full calculation results of level shifts and widths of the  $g_{9/2}$  state, with respect to the optical potential parameters and density profiles. The second to the fifth columns, the shift and width for  $^{40}\text{Ca}$ , the counterparts for  $^{48}\text{Ca}$  are provided, with the Type I potential. The sixth to tenth, eleventh to fourteenth columns are dedicated for Type II and Type III potential in the same order. The result of 3pF density for  $^{40}\text{Ca}$  is exhibited in ‘‘3pF-2.0’’ line.

$g_{9/2}$	Type I				Type II				Type III			
	$^{40}\text{Ca}$		$^{48}\text{Ca}$		$^{40}\text{Ca}$		$^{48}\text{Ca}$		$^{40}\text{Ca}$		$^{48}\text{Ca}$	
	$\varepsilon(\text{eV})$	$\Gamma(\text{eV})$										
3pF-2.0	2.85	43.4	3.56	53.9	2.85	43.4	18.5	40.3	25.9	14.6	31.1	15.3
3pF-2.5	–	–	3.79	55.3	–	–	20.5	40.7	–	–	31.8	15.7
3pF-3.0	–	–	4.04	56.8	–	–	22.5	41.1	–	–	32.6	16.0
SLy4	2.60	30.0	4.82	40.9	–1.52	31.8	22.1	30.9	21.4	11.57	29.3	14.9
SLy5	2.56	29.9	4.72	41.8	–1.58	31.7	22.9	31.7	21.3	11.50	29.4	14.8
SkM*	2.49	31.0	4.76	40.6	–2.06	32.9	21.2	30.3	21.6	11.56	29.1	14.9
SAMi	2.45	27.7	4.60	41.8	–1.42	29.4	24.1	31.6	20.4	11.01	29.2	14.6
SGII	2.20	29.1	4.35	39.3	–2.21	30.8	20.3	29.8	20.5	10.95	28.1	14.2
UNEDF0	2.35	31.2	4.45	45.6	–2.31	32.7	28.6	34.1	21.6	11.40	30.3	15.0
UNEDF1	2.10	29.7	3.99	44.3	–2.17	30.8	28.3	33.8	20.7	10.90	29.2	14.3
UNEDF2	2.10	28.5	4.06	41.0	–1.93	29.5	25.0	31.1	20.2	10.69	28.3	14.1
HFB9	2.41	30.8	4.65	41.3	–2.27	32.5	22.9	31.0	21.5	11.41	29.2	14.7

TABLE X. The same with Table IX, but for  $g_{7/2}$  state.

$g_{7/2}$	Type I				Type II				Type III			
	$^{40}\text{Ca}$		$^{48}\text{Ca}$		$^{40}\text{Ca}$		$^{48}\text{Ca}$		$^{40}\text{Ca}$		$^{48}\text{Ca}$	
	$\varepsilon(\text{eV})$	$\Gamma(\text{eV})$										
3pF2.0	2.83	44.0	3.55	54.7	2.83	44.0	18.7	40.9	26.2	14.8	31.5	15.5
3pF2.5	–	–	3.79	56.1	–	–	20.8	41.3	–	–	32.2	15.9
3pF3.0	–	–	4.03	57.7	–	–	22.8	41.7	–	–	33.0	16.2
SLy4	2.59	30.4	4.83	41.5	–1.61	32.2	22.3	31.4	21.7	11.72	29.6	15.1
SLy5	2.55	30.3	4.73	42.4	–1.66	32.1	23.2	32.2	21.6	11.65	29.8	15.0
SkM*	2.47	31.4	4.76	41.2	–2.16	33.3	21.5	30.8	21.9	11.72	29.4	15.1
SAMi	2.43	28.1	4.60	42.4	–1.50	29.8	24.4	32.0	20.6	11.15	29.6	14.8
SGII	2.18	29.5	4.35	39.8	–2.31	31.2	20.6	30.2	20.8	11.09	28.4	14.4
UNEDF0	2.33	31.6	4.45	46.3	–2.41	33.1	29.0	34.6	21.8	11.55	30.7	15.2
UNEDF1	2.07	30.1	3.98	44.9	–2.27	31.2	28.7	34.3	20.9	11.04	29.6	14.5
UNEDF2	2.07	28.8	4.06	41.6	–2.02	29.9	25.4	31.5	20.4	10.83	28.6	14.3
HFB9	2.39	31.2	4.65	41.9	–2.37	32.9	23.2	31.5	21.7	11.56	29.5	14.9

TABLE XI. The same with Table IX, but for  $h_{11/2}$  state.

$h_{11/2}$	Type I				Type II				Type III			
	$^{40}\text{Ca}$		$^{48}\text{Ca}$		$^{40}\text{Ca}$		$^{48}\text{Ca}$		$^{40}\text{Ca}$		$^{48}\text{Ca}$	
	$\varepsilon(\text{eV})$	$\Gamma(\text{eV})$										
3pF2.0	-0.011	0.121	-0.017	0.170	-0.011	0.121	0.048	0.155	0.084	0.058	0.106	0.063
3pF2.5	-	-	-0.018	0.176	-	-	0.056	0.160	-	-	0.110	0.065
3pF3.0	-	-	-0.018	0.182	-	-	0.064	0.165	-	-	0.113	0.067
SLy4	-0.007	0.080	-0.007	0.121	-0.024	0.077	0.068	0.119	0.063	0.041	0.093	0.058
SLy5	-0.007	0.079	-0.008	0.125	-0.024	0.077	0.072	0.124	0.062	0.041	0.094	0.058
SkM*	-0.008	0.083	-0.007	0.120	-0.027	0.080	0.064	0.115	0.064	0.041	0.092	0.058
SAMi	-0.006	0.072	-0.008	0.125	-0.021	0.070	0.078	0.126	0.058	0.038	0.093	0.057
SGII	-0.007	0.077	-0.007	0.115	-0.025	0.074	0.061	0.112	0.060	0.038	0.088	0.055
UNEDF0	-0.008	0.084	-0.011	0.140	-0.028	0.080	0.097	0.144	0.064	0.041	0.099	0.059
UNEDF1	-0.008	0.079	-0.012	0.136	-0.026	0.075	0.097	0.143	0.060	0.038	0.094	0.056
UNEDF2	-0.007	0.075	-0.009	0.122	-0.024	0.071	0.081	0.125	0.058	0.037	0.090	0.054
HFB9	-0.008	0.083	-0.008	0.123	-0.027	0.079	0.071	0.121	0.063	0.041	0.093	0.057

TABLE XII. The same with Table IX, but for  $h_{9/2}$  state.

$h_{9/2}$	Type I				Type II				Type III			
	$^{40}\text{Ca}$		$^{48}\text{Ca}$		$^{40}\text{Ca}$		$^{48}\text{Ca}$		$^{40}\text{Ca}$		$^{48}\text{Ca}$	
	$\varepsilon(\text{eV})$	$\Gamma(\text{eV})$										
3pF2.0	-0.012	0.121	-0.017	0.170	-0.012	0.121	0.048	0.155	0.084	0.058	0.106	0.063
3pF2.5	-	-	-0.018	0.176	-	-	0.056	0.160	-	-	0.110	0.065
3pF3.0	-	-	-0.018	0.182	-	-	0.064	0.165	-	-	0.113	0.067
SLy4	-0.007	0.079	-0.007	0.121	-0.024	0.077	0.068	0.119	0.063	0.041	0.093	0.058
SLy5	-0.007	0.079	-0.008	0.125	-0.024	0.076	0.072	0.124	0.062	0.041	0.094	0.058
SkM*	-0.008	0.083	-0.007	0.120	-0.027	0.080	0.064	0.115	0.064	0.041	0.092	0.058
SAMi	-0.006	0.071	-0.008	0.125	-0.022	0.069	0.078	0.126	0.058	0.038	0.093	0.055
SGII	-0.007	0.077	-0.007	0.115	-0.026	0.073	0.061	0.112	0.059	0.038	0.088	0.055
UNEDF0	-0.008	0.084	-0.011	0.140	-0.028	0.080	0.097	0.144	0.064	0.041	0.099	0.059
UNEDF1	-0.008	0.079	-0.012	0.136	-0.026	0.074	0.097	0.143	0.060	0.038	0.094	0.056
UNEDF2	-0.007	0.075	-0.009	0.122	-0.024	0.070	0.081	0.125	0.058	0.037	0.090	0.054
HFB9	-0.008	0.083	-0.008	0.123	-0.028	0.079	0.071	0.121	0.063	0.041	0.093	0.057

- [8] T. Gaitanos and M. Kaskulov, *Nuclear Physics A* **940**, 181 (2015).
- [9] L. Adamczyk *et al.* (The STAR Collaboration), *Nature* **527**, 345 (2015).
- [10] J. Hrtánková and J. Mareš, *Nuclear Physics A* **945**, 197 (2016).
- [11] L.-Y. Dai, J. Haidenbauer, and U.-G. Meißner, *J. High Energ. Phys.* **2017**, 78.
- [12] H. Aghai-Khozani, A. Bianconi, M. Corradini, R. Hayano, M. Hori, M. Leali, E. Lodi Rizzini, V. Mascagna, Y. Murakami, M. Prest, E. Vallazza, L. Venturilli, and H. Yamada, *Nuclear Physics A* **970**, 366 (2018).
- [13] J. Hrtánková and J. Mareš, *Nuclear Physics A* **969**, 45 (2018).
- [14] M. Germann, S. Patra, J.-P. Karr, L. Hilico, V. I. Korobov, E. J. Salumbides, K. S. E. Eikema, W. Ubachs, and J. C. J. Koelemeij, *Phys. Rev. Res.* **3**, L022028 (2021).
- [15] N. Paul, G. Bian, T. Azuma, S. Okada, and P. Indelicato, *Phys. Rev. Lett.* **126**, 173001 (2021).
- [16] J. Haidenbauer and U.-G. Meißner, *EPJ Web Conf.* **258**, 06002 (2022).
- [17] C. J. Batty, E. Friedman, H. J. Gils, and H. Rebel, in *Advances in Nuclear Physics*, edited by J. W. Negele and E. Vogt (Springer US, Boston, MA, 1989) pp. 1–188.
- [18] S. Wycech, J. Skalski, R. Smolańczuk, J. Dobaczewski, and J. R. Rook, *Phys. Rev. C* **54**, 1832 (1996).
- [19] P. Lubiński, J. Jastrzębski, A. Trzcińska, W. Kurcewicz, F. J. Hartmann, W. Schmid, T. von Egidy, R. Smolańczuk, and S. Wycech, *Phys. Rev. C* **57**, 2962 (1998).
- [20] R. Schmidt, A. Trzcińska, T. Czosnyka, T. von Egidy, K. Gulda, F. J. Hartmann, J. Jastrzębski, B. Ketzer, M. Kisieliński, B. Kłos, W. Kurcewicz, P. Lubiński, P. Napiorkowski, L. Pieńkowski, R. Smolańczuk, E. Widmann, and S. Wycech, *Phys. Rev. C* **67**, 044308 (2003).
- [21] J. Jastrzębski, A. Trzcińska, P. Lubiński, B. Kłos, F. J. Hartmann, T. von EGIDY, and S. Wycech, *Int. J. Mod. Phys. E* **13**, 343 (2004).
- [22] B. Kłos, S. Wycech, A. Trzcińska, J. Jastrzębski, T. Czosnyka, M. Kisieliński, P. Lubiński, P. Napiorkowski, L. Pieńkowski, F. J. Hartmann, B. Ketzer, R. Schmidt, T. Von Egidy, J. Cugnon, K. Gulda, W. Kurcewicz, and E. Widmann, *Phys. Rev. C* **69**,

- 044311 (2004).
- [23] B. Kłos *et al.*, Phys. Rev. C **76**, 014311 (2007).
- [24] S. Wycech, F. J. Hartmann, J. Jastrzębski, B. Kłos, A. Trzcińska, and T. von Egidy, Phys. Rev. C **76**, 034316 (2007).
- [25] E. Friedman, Hyperfine Interact. **193**, 33 (2009).
- [26] A. Trzcińska (for PS209 collaboration), Hyperfine Interact. **194**, 271 (2009).
- [27] F. Ficek, P. Fadeev, V. V. Flambaum, D. F. Jackson Kimball, M. G. Kozlov, Y. V. Stadnik, and D. Budker, Phys. Rev. Lett. **120**, 183002 (2018).
- [28] T. Aumann *et al.* (PUMA Collaboration), Eur. Phys. J. A **58**, 88 (2022).
- [29] S. Wycech, F. J. Hartmann, H. Daniel, W. Kanert, H. S. Plendl, T. von Egidy, J. J. Reidy, M. Nicholas, L. A. Redmond, H. Koch, A. Kreissl, H. Poth, and D. Rohmann, Nuclear Physics A **561**, 607 (2019).
- [30] D. Gotta, D. F. Anagnostopoulos, M. Augsburg, G. Borchert, C. Castelli, D. Chatellard, J. P. Egger, P. El-Khoury, H. Gorke, P. Hauser, P. Indelicato, K. Kirch, S. Lenz, N. Nelms, K. Rashid, Th. Siems, and L. M. Simons, Nuclear Physics A **660**, 283 (1999).
- [31] D. Gotta, Progress in Particle and Nuclear Physics **52**, 133 (2004).
- [32] L. S. Kisslinger, Phys. Rev. **98**, 761 (1955).
- [33] M. Ericson and T. E. O. Ericson, Annals of Physics **36**, 323 (1966).
- [34] H. Nishimura and T. Fujita, Physics Letters B **60**, 413 (1976).
- [35] C. J. Batty, Nuclear Physics A **372**, 433 (1981).
- [36] J. Côté, M. Lacombe, B. Loiseau, B. Moussallam, and R. V. Mau, Phys. Rev. Lett. **48**, 1319 (1982).
- [37] C. J. Batty, Physics Letters B **189**, 393 (1987).
- [38] C. J. Batty, E. Friedman, and A. Gal, Nuclear Physics A **592**, 487 (1995).
- [39] E. Friedman and A. Gal, Nuclear Instruments and Methods in Physics Research Section B: Beam Interactions with Materials and Atoms **214**, 160 (2004).
- [40] E. Friedman, A. Gal, and J. Mareš, Nuclear Physics A **761**, 283 (2005).
- [41] E. Friedman, A. Gal, B. Loiseau, and S. Wycech, Nuclear Physics A **943**, 101 (2015).
- [42] P.-G. Reinhard, Rep. Prog. Phys. **52**, 439 (1989).
- [43] B. D. Serot and J. D. Walecka, in *Recent Progress in Many-Body Theories: Volume 3*, edited by T. L. Ainsworth, C. E. Campbell, B. E. Clements, and E. Krotscheck (Springer US, Boston, MA, 1992) pp. 49–92.
- [44] T. Bürvenich, I. N. Mishustin, L. M. Satarov, J. A. Maruhn, H. Stöcker, and W. Greiner, Physics Letters B **542**, 261 (2002).
- [45] I. N. Mishustin, L. M. Satarov, T. J. Bürvenich, H. Stöcker, and W. Greiner, Phys. Rev. C **71**, 035201 (2005).
- [46] A. B. Larionov, I. N. Mishustin, L. M. Satarov, and W. Greiner, Phys. Rev. C **78**, 014604 (2008).
- [47] A. B. Larionov, I. N. Mishustin, L. M. Satarov, and W. Greiner, Phys. Rev. C **82**, 024602 (2010).
- [48] T. Gaitanos, M. Kaskulov, and H. Lenske, Physics Letters B **703**, 193 (2011).
- [49] E. Friedman and A. Gal, Nuclear Physics A **899**, 60 (2013).
- [50] E. Friedman and A. Gal, Nuclear Physics A Special Issue Dedicated to the Memory of Gerald E Brown (1926-2013), **928**, 128 (2014).
- [51] E. Friedman, EPJ Web Conf. **199**, 01013 (2019).
- [52] E. Friedman and A. Gal, Physics Letters B **792**, 340 (2019).
- [53] A. Trzcińska *et al.* (PS209 collaboration), Nuclear Physics A **692**, 176 (2001).
- [54] F. J. Hartmann, R. Schmidt, B. Ketzer, T. von Egidy, S. Wycech, R. Smolańczuk, T. Czosnyka, J. Jastrzębski, M. Kisieliński, P. Lubiński, P. Napiorkowski, L. Pieńkowski, A. Trzcińska, B. Kłos, K. Gulda, W. Kurcewicz, and E. Widmann, Phys. Rev. C **65**, 014306 (2001).
- [55] T. Naito, T. Oishi, H. Sagawa, and Z. Wang, Phys. Rev. C **107**, 054307 (2023).
- [56] J. Zenihiro, H. Sakaguchi, S. Terashima, T. Uesaka, G. Hagen, M. Itoh, T. Murakami, Y. Nakatsugawa, T. Ohnishi, H. Sagawa, H. Takeda, M. Uchida, H. P. Yoshida, S. Yoshida, and M. Yosoi, (2018), arXiv:1810.11796 [nucl-ex, nucl-th].
- [57] J. Zenihiro, T. Uesaka, H. Sagawa, and S. Yoshida, Progress of Theoretical and Experimental Physics **2021**, 023D05 (2021).
- [58] H. Sagawa, S. Yoshida, T. Naito, T. Uesaka, J. Zenihiro, J. Tanaka, and T. Suzuki, Physics Letters B **829**, 137072 (2022).
- [59] C. Garcia-Recio, J. Nieves, and E. Oset, Nuclear Physics A **547**, 473 (1992).
- [60] R. Schmidt, F. J. Hartmann, T. von Egidy, T. Czosnyka, J. Iwanicki, J. Jastrzębski, M. Kisieliński, P. Lubiński, P. Napiorkowski, L. Pieńkowski, A. Trzcińska, J. Kulpa, R. Smolańczuk, S. Wycech, B. Kłos, K. Gulda, W. Kurcewicz, and E. Widmann, Phys. Rev. C **58**, 3195 (1998).
- [61] A. Krasznahorkay, M. Fujiwara, P. van Aarle, H. Akimune, I. Daito, H. Fujimura, Y. Fujita, M. N. Harakeh, T. Inomata, J. Jänecke, S. Nakayama, A. Tamii, M. Tanaka, H. Toyokawa, W. Uijen, and M. Yosoi, Phys. Rev. Lett. **82**, 3216 (1999).
- [62] A. Trzcińska, J. Jastrzębski, P. Lubiński, F. J. Hartmann, R. Schmidt, T. von Egidy, and B. Kłos, Phys. Rev. Lett. **87**, 082501 (2001).
- [63] B. C. Clark, L. J. Kerr, and S. Hama, Phys. Rev. C **67**, 054605 (2003).
- [64] H. De Vries, C. W. De Jager, and C. De Vries, Atomic Data and Nuclear Data Tables **36**, 495 (1987).
- [65] T. H. R. Skyrme, Nuclear Physics **9**, 615 (1958).
- [66] D. Vautherin and D. M. Brink, Phys. Rev. C **5**, 626 (1972).
- [67] G. Colò, Adv. Phys. X **5**, 1740061 (2020).
- [68] H. Fujioka, private communication.
- [69] C. Smorra *et al.*, Nature **550**, 371 (2017).
- [70] L. W. Fullerton and G. A. Rinker, Phys. Rev. A **13**, 1283 (1976).
- [71] E. Borie, Phys. Rev. A **28**, 555 (1983).
- [72] M. Pignone, M. Lacombe, B. Loiseau, and R. Vinh Mau, Phys. Rev. C **50**, 2710 (1994).
- [73] B. El-Bennich, M. Lacombe, B. Loiseau, and R. Vinh Mau, Phys. Rev. C **59**, 2313 (1999).
- [74] B. El-Bennich, M. Lacombe, B. Loiseau, and S. Wycech, Phys. Rev. C **79**, 054001 (2009).
- [75] Tables of Nuclear Data, <https://www.ndc.jaea.go.jp/NuC/>.
- [76] E. Chabanat, P. Bonche, P. Haensel, J. Meyer, and R. Schaeffer, Nuclear Physics A **635**, 231 (1998).
- [77] J. Bartel, P. Quentin, M. Brack, C. Guet, and H. B. Håkansson, Nuclear Physics A **386**, 79 (1982).
- [78] X. Roca-Maza, G. Colò, and H. Sagawa, Phys. Rev. C **86**, 031306 (2012).
- [79] N. Van Giai and H. Sagawa, Physics Letters B **106**, 379 (1981).
- [80] M. Kortelainen, T. Lesinski, J. Moré, W. Nazarewicz, J. Sarich, N. Schunck, M. V. Stoitsov, and S. Wild, Phys. Rev. C **82**, 024313 (2010).
- [81] M. Kortelainen, J. McDonnell, W. Nazarewicz, P.-G. Reinhard, J. Sarich, N. Schunck, M. V. Stoitsov, and S. M. Wild, Phys. Rev. C **85**, 024304 (2012).
- [82] M. Kortelainen, J. McDonnell, W. Nazarewicz, E. Olsen, P.-G. Reinhard, J. Sarich, N. Schunck, S. M. Wild, D. Davesne, J. Erler, and A. Pastore, Phys. Rev. C **89**, 054314 (2014).

- [83] S. Goriely, M. Samyn, J. M. Pearson, and M. Onsi, Nuclear Physics A **750**, 425 (2005).
- [84] J. Dobaczewski, H. Flocard, and J. Treiner, Nuclear Physics A **422**, 103 (1984).
- [85] A. Gal, E. Friedman, and C. J. Batty, Nuclear Physics A **606**, 283 (1996).